Earthline Journal of Chemical Sciences
E-ISSN: 2581-9003; CODEN: EJCSB4
Volume 12, Number 4, 2025, Pages 379-396
https://doi.org/10.34198/ejcs.12425.379396

Molecular and crystal engineering of a semicarbazide–ketone condensate: A multitechnique characterization

Fatou Dieng

Laboratoire de Chimie Minérale et Analytique, Département de Chimie, Faculté des Sciences et Techniques, Université Cheikh Anta Diop, Dakar, Sénégal

Papa Aly Gueye

Laboratoire de Chimie Minérale et Analytique, Département de Chimie, Faculté des Sciences et Techniques, Université Cheikh Anta Diop, Dakar, Sénégal

Mouhamadou Birame Diop

Laboratoire de Chimie Minérale et Analytique, Département de Chimie, Faculté des Sciences et Techniques, Université Cheikh Anta Diop, Dakar, Sénégal
e-mail: mouhamadoubdiop@gmail.com

Adrienne Ndiolene

Laboratoire de Chimie Minérale et Analytique, Département de Chimie, Faculté des Sciences et Techniques, Université Cheikh Anta Diop, Dakar, Sénégal

Mouhamadou Sembene Boye

Département de Physique Chimie, Faculté des Sciences et Technologies de l'éducation et de la formation, Boulevard Habib Bourguiba, Université Cheikh Anta Diop, 5036 Fann-Dakar, Sénégal

Shova Sergiu

Inorganic Polymers Department, "Petru Poni" Institute of Macromolecular Chemistry, Alea Gr. Ghica Voda 41A, Iasi 700487, Romania

Aminata Diassé-Sarr

Laboratoire de Chimie Minérale et Analytique, Département de Chimie, Faculté des Sciences et Techniques, Université Cheikh Anta Diop, Dakar, Sénégal

Abstract

The studied organic compound, namely (2Z)-2-(2-chloro-1-phenylethylidene)hydrazine-1-carboxamide was synthesized *via* a condensation reaction between semicarbazide hydrochloride and α-chloroacetophenone, affording a hydrazone–carboxamide derivative in good yield. Its structure was elucidated using single crystal X-ray crystallography, ATR-FTIR, ^{1}H NMR, ^{13}CNMR, DEPT 135°, and Hirshfeld surface analysis. The compound [C_6H_5-$C(CH_2Cl)N$=NH-$C(O)NH_2$] (**1**), crystallizes in the monoclinic space group $P2_1/C$ with Z = 4, a = 10.6213(8) Å, b = 7.2518(5) Å, c = 13.6791(9) Å, β = 101.018(7)° and V = 1034.19(13) Å^3. ATR-FTIR and NMR

Received: July 28, 2025; Accepted: September 2, 2025; Published: September 11, 2025

Keywords and phrases: single crystal X-ray, semicarbazide condensation, spectroscopic characterization, Hirshfeld surface analysis, supramolecular assembly.

*Corresponding author

data confirmed the presence of a monosubstituted aromatic ring, a chloromethyl side chain, and a conjugated hydrazone–amide moiety. Single-crystal X-ray analysis revealed typical metrics consistent with a C=N double bond and a urea-like C=O(–NH_2) fragment. In the crystal, molecules are linked by directional N–H···O and N–H···N hydrogen bonding patterns, giving rise to centrosymmetric $R_2^2(8)$ dimers, extended $R_2^2(9)$ rings, and larger $R_4^6(14)$ macrocyclic assemblies, generating a two-dimensional supramolecular network parallel to the (100) plane. Hirshfeld surface analysis supported the dominance of hydrogen bonding in the packing arrangement and confirmed the absence of significant π···π stacking interactions. These results achieve the critical role of hydrogen bonding in directing the crystal architecture and stabilizing the structure.

1. Introduction

Over the past two decades, semicarbazones and related hydrazone compounds have played a key role in the design of countless molecules with interesting functional diversity. Their versatile scaffolds, owing to the presence of the C=N–NH–C(O)–NH_2 moiety, allow for both a high synthetic flexibility and intriguing biological, optical, and electronic properties [1–3]. Such features made them attractive frameworks in various fields as medicinal chemistry, materials science, and coordination chemistry. Moreover, they aroused remarkable antimicrobial, anticancer, antimalarial, and neuroprotective properties which are improved through transition metals or structural modification [4–6]. A high effectiveness against *Trypanosomatids*, *Plasmodium spp*, and cancer cell lines have been reported for thiosemicarbazone and semicarbazone derivatives, acting through mechanisms as reactive oxygen species generation and ribonucleotide reductase inhibition [4, 6]. For example, promising in vitro EGFR inhibitions with cytotoxicity toward colon and breast cancer cells were recorded for some benzothiazoletriazolehydrazone hybrids [7].

Besides their biomedical relevance area, aromatic and conjugated hydrazones frameworks have well shown nonlinear optical (NLO) and photochromic properties. Indeed, crystalline nitrophenyl hydrazone afford a very large second harmonic generation (SHG) responses in comparison to urea, making hydrazones' class of compound incommensurately promising applications in photonics, optical computing and sensing technologies [8]. Furthermore, the potential of hydrazone-linked covalent organic frameworks (COFs) in energy conversion and solar-to-fuel strategies, has been showcased by applying to some of them to visible light driven photocatalytic hydrogen generation [9].

In another hand, semicarbazone-type ligands play a key role in coordination acting as versatile chelators for transition metals (Co^{2+}, Zn^{2+}, Cu^{2+}, Ni^{2+}), growing complexes with excellent catalytic, antimicrobial and material-functional applications [6]. The DFT and NBO computational recent investigations on such systems, have further clarified their electronic structure, charge delocalization and reactivity, describing their HOMO–LUMO gaps, electrophilicity indices and frontier orbital distributions as critical determinants of their functional behaving [10].

In this work, a new semicarbazide–ketone hydrazone was synthesized *via* a mild condensation process reaction and fully structurally characterized on the basis of a comprehensive approach that combines FTIR in ATR mode and NMR spectroscopies, single-crystal X-ray diffraction and Hirshfeld surface analysis. The resulting molecular and supramolecular features describe a rich hydrogen-bonded architecture consistent with the formation of fused ring motifs, highlighting the structural potential of such materials.

2. Materials and Methods

2.1. General

Chemicals (α-Chloroacetophenone, semicarbazide hydrochloride, sodium hydroxide) were obtained from Sigma Aldrich and used without any prior purification. The methanol solvent was purchased from Aldrich company and used as received. The NMR spectra of the compound were recorded on a Bruker Avance 400 MHz spectrometer with a band-end fluorine observation (BBFO) sensor in deuterated acetone at the Aix-Marseille University (France). The X-ray crystallographic data for **1** were collected using a Rigaku diffractometer at the Institute of Macromolecular Chemistry (Romania). The Hirsfeld surface analyses were obtained using CrystalExplorer program version 21.5. The crystal was held at 293 K during data collection. The structure was solved using SHELXT and refined by SHELXL programs.

2.2. Synthesis of [C_6H_5-$C(CH_2Cl)N$=NH-$C(O)NH_2$] (1)

The title compound was synthesized *via* a condensation reaction between semicarbazide hydrochloride (24 mmol; 2.677 g) and α-chloroacetophenone (24 mmol, 3.708 g). Semicarbazide hydrochloride was preliminary dissolved in 20 mL of methanol, resulting in a suspension. To neutralize the hydrochloric acid liberated from the salt, a methanolic solution of sodium hydroxide (12 mmol, 0.48 g in 5 mL MeOH) was added dropwise under constant magnetic stirring. The resulting mixture became homogenous upon neutralization. Subsequently, a solution of α-chloroacetophenone (24 mmol; 3.708 g) in 10 mL of methanol was introduced into the reaction medium, followed by the addition of two drops of glacial acetic acid to catalyze the condensation. The reaction mixture was then stirred under reflux at 60 °C for 2 hours. Upon completion, the reaction was left to slowly evaporate at room temperature over a period of two days, yielding colorless single crystals suitable for X-ray diffraction. The isolated product was obtained in a 75% yield (Scheme 1).

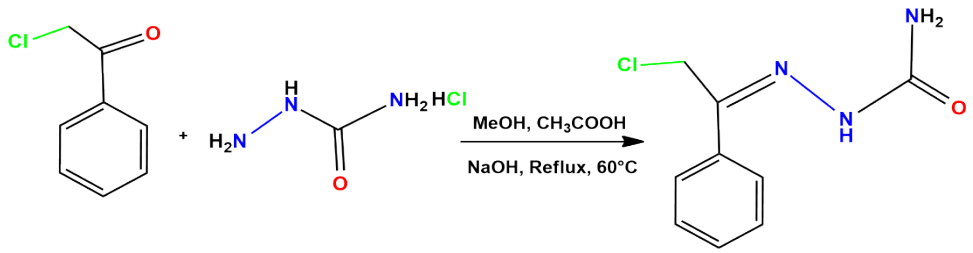

Scheme 1: Reaction of the formation of the Schiff base **1**.

2.3. X-ray Crystallography

The X-ray crystallographic data of **1** were collected using a Rigaku diffractometer operating at T = 293(2) K. Data was measured using φ and ω scans of 0.5° using Mo$K\alpha$ radiation (λ = 0.71073 Å) under the program CrysAlisPro 1.171.44.88a [11]. Cell parameters were determined and refined using the program CrysAlisPro 1.171.44.88a [11]. CrysAlisPro 1.171.44.88a [11] program was also used for data reduction. Empirical absorption correction using spherical harmonics, implemented in SCALE3 ABSPACK scaling algorithm was applied using CrysAlisPro 1.171.44.88a [11].The structure was solved by intrinsic phasing using SHELXT [12] and refined using least-squares minimization with SHELXL [13].

Programs used for the representation of the molecular and crystal structures: Olex2 [14] and CrystalExplorer [15]. Crystal data, data collection and structure refinement details for **1** are summarized in Table 1.

CCDC 2476340 (**1**) contains the supplementary crystallographic data for this paper. Copies of these data can be obtained free of charge from the Cambridge Crystallographic Data Centre (CCDC), 12 Union Road, Cambridge CB2 1EZ, UK (fax: int. Code +44 1223 336 033; e-mail: deposit@ccdc.cam.ac.uk or www: http://www.ccdc.cam.ac.uk).

Table 1. Crystal data and structure refinement of compound **1**

Parameters	**1**
Empirical formula	$C_9H_{10}N_3OCl$
Formula weight	211.65
Temperature/K	293(2)
Crystal system	Monoclinic
Space group	$P2_1/c$
a/Å	10.6213(8)
b/Å	7.2518(5)
c/Å	13.6791(9)
α/°	90
β/°	101.018(7)
γ/°	90
Volume/Å^3	1034.19(13)
Z	4
ρ_{calc}g/cm^3	1.359
μ/mm^{-1}	0.340
F(000)	440.0
Crystal size/mm^3	0.4 × 0.2 × 0.2
Radiation	MoKα (λ = 0.71073)
2Θ range for data collection/°	3.906 to 58.278
Index ranges	$-14 \le h \le 12$ $-9 \le k \le 9$ $-16 \le l \le 18$
Reflections collected	7168
Independent reflections	2451 [R_{int} = 0.0324, R_{sigma} = 0.0402]

Parameters	**1**
Data/restraints/parameters	2451/0/136
Goodness-of-fit on F^2	1.034
Final R indexes [I>=2σ (I)]	R_1 = 0.0589, wR_2 = 0.1346
Final R indexes [all data]	R_1 = 0.0954, wR_2 = 0.1554
Largest diff. peak/hole / e $Å^{-3}$	0.333/-0.364

R1 = Σ(||F_o|-|F_c||)/ Σ |F_o|; wR2 = [Σ w(F_o^2-F_c^2)^2/ Σ [w(F_o^2)^2]$^{1/2}$ where w = 1/[$σ^2$(F_o^2) + 0.3215P+(0.0616P)^2]; [c] goodness of fit = [Σ w(F_o^2-F_c^2)^2/(N_o-N_v)]$^{1/2}$.

3. Results and Discussion

The formation of compound **1** follows a nucleophilic condensation between the hydrazine moiety of semicarbazide and the carbonyl group of *α*-chloroacetophenone, giving rise to a hydrazone derivative (Eq. 1). The addition of sodium hydroxide aimed to neutralize semicarbazide hydrochloride, thereby generating free nucleophilic species in situ. Subsequent acid-catalyzed condensation, promoted by a catalytic amount of glacial acetic acid, assisted the efficient formation of the imine (C=N) bond, typical of Schiff base growth as encountered in the literature [16–18]. Because of their synthetic accessibility, chemical stability, and electronic tunability, hydrazone's family compounds are very useful in organic synthesis, coordination chemistry, and medicinal chemistry [6, 10], where the C=N linkage behaves as a reactive site or coordination center.

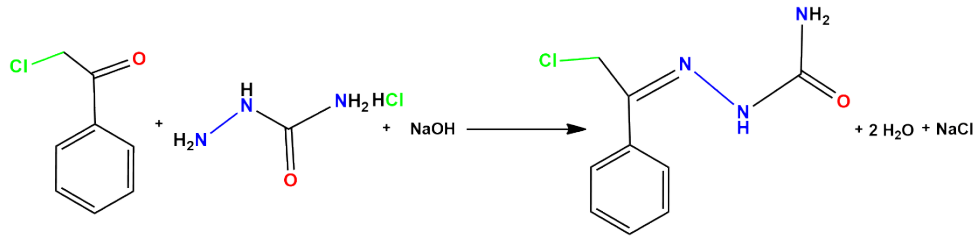

The structure of compound **1** was elucidated by combination of several approaches *i.e.* spectroscopic analysis (FTIR, ^{1}H NMR, ^{13}C NMR, and DEPT experiments), single-crystal X-ray diffraction and Hirshfeld surface analysis.

The ATR-FTIR spectrum (Figure S1) of the title compound was recorded in the 4000–450 cm^{-1} region and exhibits key absorption bands consistent with the hydrazone, amide, aromatic, and alkyl chloride functionalities. The absorption bands observed at 3447.62 cm^{-1} and 3340.74 cm^{-1} characteristic of N–H stretching vibrations are attributed to the hydrazine moiety (–NH–N=) and the amide group (–$CONH_2$), both of which are able to govern hydrogen bond interactions and often display broadened bands in this region [18]. The broad band around 3041.38 cm^{-1} corresponds to the aromatic C–H stretching, confirming the presence of the monosubstituted phenyl ring. Prominently, the amide carbonyl (C=O) group appears at 1693.00 cm^{-1}, with the

nearby vibration recorded at 1665.93 cm^{-1} is assigned to the C=N stretching vibration of the hydrazone linkage. These two pairing bands confirm the presence of conjugated carbonyl and imine functionalities, which are central to the structural identity of the compound [10]. The several bands encountered in the region 1602.58–1434.74 cm^{-1} correspond to C=C stretching and in-plane C–H bending vibrations within the aromatic ring. The vibration at 1602.58 cm^{-1} is particularly indicative of the aromatic C=C skeleton. The absorptions in the 1300–1100 cm^{-1} region, at 1258.29 cm^{-1}, 1163.3 cm^{-1}, and 1144.96 cm^{-1} are assigned to C–N stretching vibrations, typically observed in amides and hydrazone containing derivatives [6]. Lower frequency band vibrations at 572.02 cm^{-1} and 488.24 cm^{-1} are attributed to C–Cl stretching, corroborating the presence of the chloromethyl group (–CH_2Cl). The spectrum also features multitude strong bands between 839.95 and 688.36 cm^{-1}, consistent with out of plane bending of aromatic C–H bonds.

The ^1H NMR spectrum of the studied compound (Figure S2), recorded in acetone-d_6, displays four distinct signals, corresponding to non-equivalent proton environments in the molecule. The multiplet centered at 7.42 ppm is attributed to the five aromatic protons of a monosubstituted benzene ring. The chemical shift and pattern are typical for such environments, often observed between 7.0 and 7.5 ppm [19]. The singlet at 9.15 ppm corresponds to the NH proton of the hydrazone fragment (–C=N–NH–). This highly deshielded signal appears within the expected range for hydrazone NH protons, which typically resonate between 8.5 and 10.5 ppm, particularly in solvents like acetone-d_6 where hydrogen bonding interactions are weakly present [20]. The singlet at 5.63 ppm is assigned to the NH_2 group of the terminal amide moiety. Indeed, in acetone-d_6, amide NH_2 signals often appear slightly upfield compared to DMSO-d_6 due to weaker hydrogen bonding interactions, with values often ranging from 5.0 to 6.5 ppm [21]. The singlet at 4.57 ppm is attributed to the methylene protons (CH_2) of the CH_2Cl group, appearing in the expected region between 3.5 and 4.5 ppm. The slight downfield shift here is likely due to electrons withdrawing effects from both the adjacent chlorine atom and conjugated imine [22].

Although compound **1** contains eight carbon atoms, within the spectral window of the ^{13}C NMR experiment (0–150 ppm) only seven distinct resonances are observed (Figure S3). This apparent conflict arises from partial overlap of the aromatic carbon signals, which is common in monosubstituted phenyl rings due to similar electronic environments and magnetic equivalence of certain positions. The seven distinct carbon signals are consistent with the number of magnetically non-equivalent carbon environments. The five signals between 125.98 and 129.50 ppm are attributed to the aromatic CH carbons of the benzene ring, in accordance with literature values for protonated sp^2 carbons within substituted phenyl rings. The signal at 33.42 ppm is assigned to the methylene carbon (CH_2) of the CH_2Cl fragment, whose position is in good agreement with known values for terminal aliphatic carbons bearing halogen substituents (30–50 ppm). The signal at 48.85 ppm is attributed to the quaternary benzylic carbon, connecting the aromatic ring, the CH_2Cl group, and the hydrazone nitrogen.It is noteworthy to outline that the spectral window of the ^{13}C NMR experiment, limited to 0–150 ppm, excludes the typical resonance region of amide carbonyl carbons (160–180 ppm). As result, the expected carbonyl signal could not be observed in the spectrum, and its absence should not be interpreted as evidence of non-existence. The carbonyl carbon is still expected to appear within its conventional range [22], however experimental confirmation would require acquisition over a broader spectral window.

The DEPT 135° spectrum (Figure S4) reveals six distinct resonances: five in positive phase, and one in negative phase. The five positive-phase signals correspond to the five aromatic CH carbons. The single negative-phase signal observed at 33.38 ppm is consistent with the methylene group of the CH_2Cl group, which appears in inverted phase due to its CH_2 character. Importantly, the signal at 48.85 ppm in the ^{13}C NMR spectrum corresponding to the benzylic carbon, is absent from the DEPT 135° spectrum, confirming it is a non-

protonated quaternary center. Likewise, the carbonyl carbon (C=O) is not visible, as expected for a quaternary carbon without attached protons.

These results confirm the structure of the compound as comprised of a monosubstituted aromatic ring, a CH_2Cl side chain, and a hydrazone–carboxamide moiety, with spectral features entirely consistent with the proposed molecular framework.

Compound **1** crystalized as clear intense colorless prism-like crystals in the centrosymmetric monoclinic space group $P2_1/C$ with 4 molecules per unit cell. The asymmetric unit is comprised of one molecule and is depicted in Figure 1.

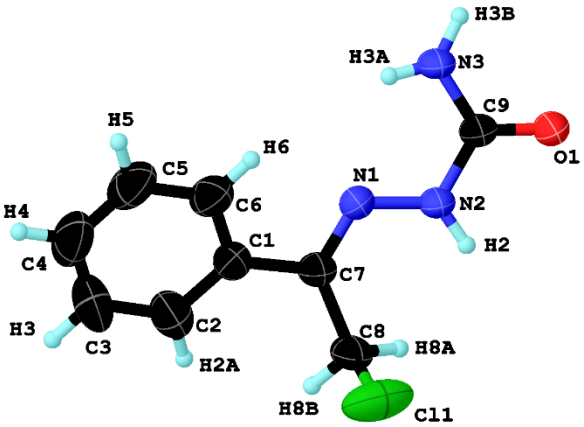

Figure 1. View of the asymmetric unit of **1** showing 50% probability ellipsoids for atoms and the crystallographic numbering scheme [atom color code: H, turquoise; C, black; N, blue; O, red; Cl, green].

The aromatic ring shows C–C bond lengths ranging from 1.372(5) to 1.391(3) Å, and internal C–C–C angles between 118.2(2)° and 120.7(3)°, consistent with typical characteristic values within regularly substituted benzene ring, with minimal deviation from ideal hexagonal arrangement, and closely match those observed in similar mono-substituted phenyl derivatives [23].The benzylic C–C bond between the phenyl ring and the adjacent carbon atom of 1.482(3) Å, is in accordance with standard sp^2–sp^3 bond distances, often found in the range 1.48–1.50 Å for phenyl–alkyl junctions [24].The C=N double bond length of 1.286(3) Å (N1–C7) is typical for Schiff base-type imines, with reported literature values ranging between 1.27 and 1.30 Å depending on the conjugation and substitution [25]. The adjacent N1–N2 bond length of 1.370(3) Å is also within the expected range for N–N single bonds in hydrazone derivatives (1.36–1.38 Å) [26], supporting the hydrazone nature of the linkage. Similar geometrical features have also been observed in related hydrazones which describe extended conjugation [27]. The C9–O1 bond length (Table 2), is clearly consistent with a carbonyl (C=O) double bond in an amide or urea-like environment, where literature values are encountered within 1.22–1.24 Å [28, 29]. The adjacent C9–N3 (1.336(3) Å) and C9–N2 (1.368(3) Å) bond lengths reflect partial double bond character due to a π delocalization, as observed in symmetrical urea or semicarbazide-type derivatives [30]. Such bond metrics are commonly reported for hydrogen-bonded urea frameworks [31, 32].Similar values have also been confirmed in some recently reported urazole-based hydrazone–amide hybrids [33].The C8–Cl1 bond value of 1.761(3) Å is slightly elongated but still within the typical range for alkyl chlorides, often between 1.75 and 1.78 Å [34]. The angles at the hydrazone junction around N1 and C7 appearing between 118° and 124° (Table 2), are consistent with a planar, conjugated –C=N–NH– system, promoting π-delocalization [26, 27]. The angles around the carbonyl carbon C9 (see Table 2 for details) reflect the sp^2 hybridization of the carbon as well as the partial delocalization of electron density over the amide group.The bond angles around the C7 benzylic carbon (see Table 2 for details) deviate slightly from the ideal

tetrahedral geometry, yet suggesting planarization because of conjugation with the imine nitrogen and steric compromise of the neighboring substituents.

The geometric parameters strongly ascertain a delocalized electronic structure of the molecule and are in accordance with metrics encountered in recent structural investigations involving urea and hydrazone-containing materials [28–34].

Table 2. Selected prominent geometric parameters (Å, °) for compounds **1**.

1			
Atom-Atom	Bond length	Atom-Atom	Bond length
Cl1–C8	1.761 (3)	C1–C2	1.387 (4)
O1–C9	1.232 (3)	C7–C8	1.504 (3)
N1–N2	1.370 (3)	C1–C6	1.391 (3)
N1–C7	1.286 (3)	C6–C5	1.385 (4)
N2–C9	1.368 (3)	C2–C3	1.379 (4)
N3–C9	1.336 (3)	C5–C4	1.372 (5)
C7–C1	1.482 (3)	C4–C3	1.374 (5)
1			
Atom-Atom-Atom	Angle value	Atom-Atom-Atom	Angle value
C7–N1–N2	121.32 (18)	C2–C1–C7	122.1 (2)
C9–N2–N1	118.61 (18)	C2–C1–C6	118.2 (2)
O1–C9–N2	120.25 (19)	C7–C8–Cl1	110.82 (16)
O1–C9–N3	122.5 (2)	C5–C6–C1	120.6 (3)
N3–C9–N2	117.3 (2)	C3–C2–C1	120.7 (3)
N1–C7–C1	115.61 (19)	C4–C5–C6	120.5 (3)
N1–C7–C8	124.7 (2)	C5–C4–C3	119.4 (3)
C1–C7–C8	119.67 (19)	C4–C3–C2	120.7 (3)
C6–C1–C7	119.7 (2)		

From a supramolecular perspective, the primary motif arises from intermolecular N–H···O hydrogen bonds involving the amide nitrogen (N2–H2) and the carbonyl oxygen (O1) (Figure 2, Table 3). These interactions occur between two symmetry-related molecules related by an inversion center at [0.5, 1, 0.5], resulting in the formation of discrete centrosymmetric dimers. The dimeric motif generates a classical eight-membered ring, described by the graph-set notation as $R_2^2(8)$ (Figure 2) [35], and forms the fundamental building block of the crystal structure. The dihedral angle between $R_2^2(8)$ ring plane and phenyl ring plane is of 30.2(2)°.

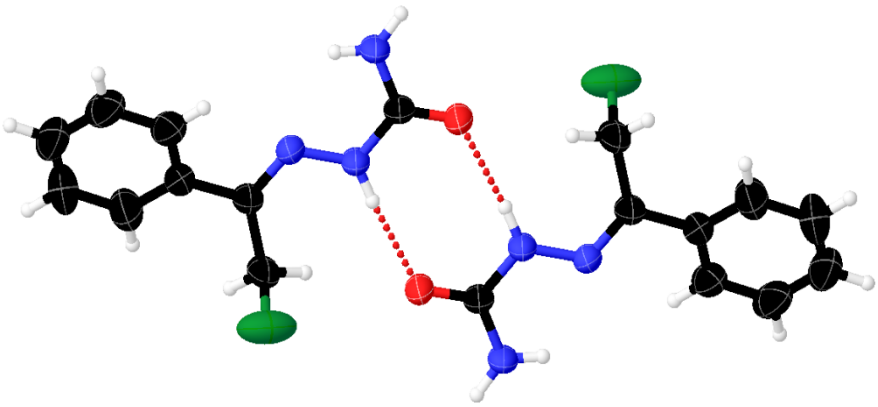

Figure 2. Ortep view of **1** showing 50% probability ellipsoids for atoms describing the organization into a dimer affording an 8-membered $R_2^2(8)$ring [atom color code: H, white; C, black; N, blue; O, red; Cl, green].

Table 3. Hydrogen-bonds and interactions geometry in the crystal of **1** [Symmetry codes: (i) −x+1, −y+2, −z+1; (ii) −x+1, y−1/2, −z+1/2; (iii) −x+1, y+1/2, −z+1/2.

D–H···A	*d*(*D*-H)	*d*(H···*A*)	*d*(*D*···*A*)	∠(*D*-H···*A*)
N2–H2···O1^{i}	0.86(3)	2.01(3)	2.868(2)	174.3(19)
N3–H3A···N1	0.82	2.15	2.636(3)	118
N3–H3A···O1^{ii}	0.82	2.47	3.044(3)	128
N3–H3B···N1^{iii}	0.87(2)	2.34(2)	3.199(3)	170(2)
C8–H8A···N2	0.97	2.50	2.855(3)	102
C8–H8A···O1^{i}	0.97	2.36	3.228(3)	149

Each molecule of the dimeric unit is further connected to two neighboring molecules *via* additional hydrogen bonding interactions, giving rise to nine-membered rings, $R_2^2(9)$, that extend the hydrogen-bonding network beyond the initial dimeric unit (Figure 3). These $R_2^2(9)$ rings are formed by N–H···O and N–H···N hydrogen bonds, particularly involving the amino group (N3–H) as donor and either the carbonyl oxygen (O1) or the imine nitrogen (N1) as acceptors. Thus, each dimer participates in four similar interactions, leading to the fusion of four $R_2^2(9)$ rings with the central $R_2^2(8)$ dimer unit (Figure 4). Hence, each dimer is surrounded by four dimers with dihedral angle between the central $R_2^2(8)$ ring and each of the four $R_2^2(8)$ rings of 54.9(8)°.

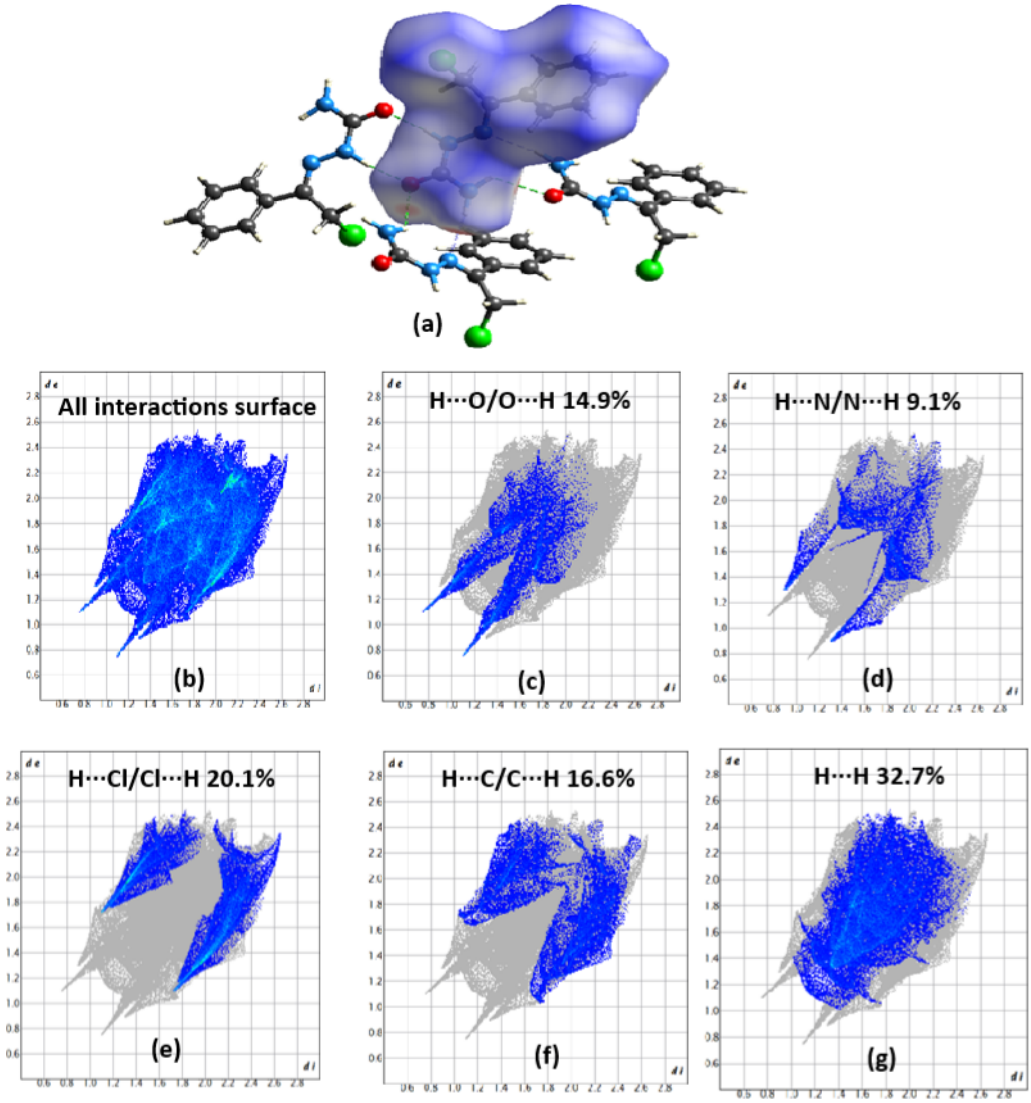

Figure 3. View of a molecule, involved in a dimeric pattern, to be surrounded with a d_{norm} decorated Hirshfeld Surface and its surrounding molecules in ball and stick presentations for compound **1** (a). The red areas indicate H···N and H···O contacts. The outline of the full fingerprint contribution (b), most important type of interactions H···O/O···H (c), H···N/N···H (d), H···Cl/Cl···H (d), H···C/C···H (f), and H···H (g) interactions in the fingerprint plot diagram.

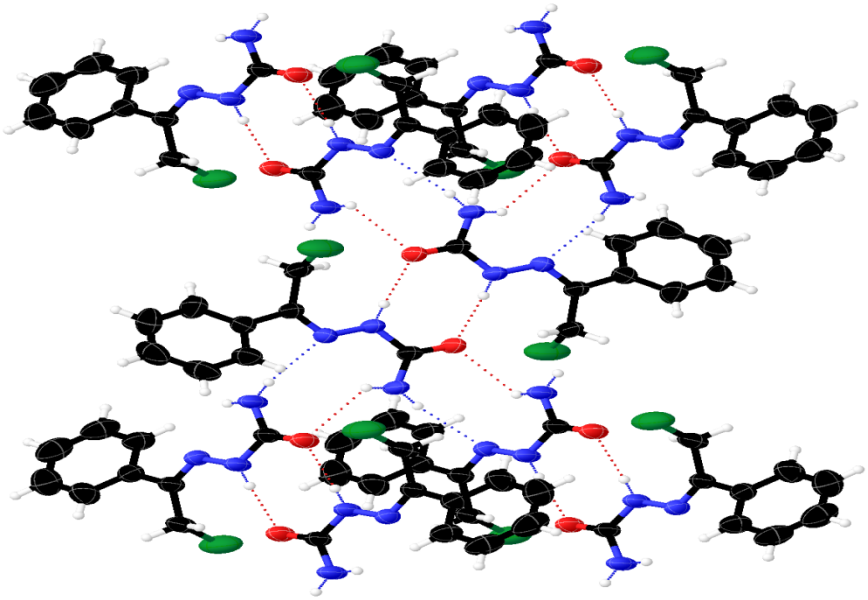

Figure 4. Ortep view of **1** (50% probability ellipsoids for atoms) describing the dimer surrounded by four neighbors affording a $R_2^2(8)$ ring fused by four $R_2^2(9)$ rings [atom color code: H, white; C, black; N, blue; O, red; Cl, green].

Close inspection of the hydrogen-bonding network reveals that this combination of interactions further interconnects two hydrogen-bonded dimers with two additional molecules from adjacent dimers, assembling into larger macrocyclic rings composed of 14 atoms, described by the graph-set $R_4^6(14)$ (Figure 5).

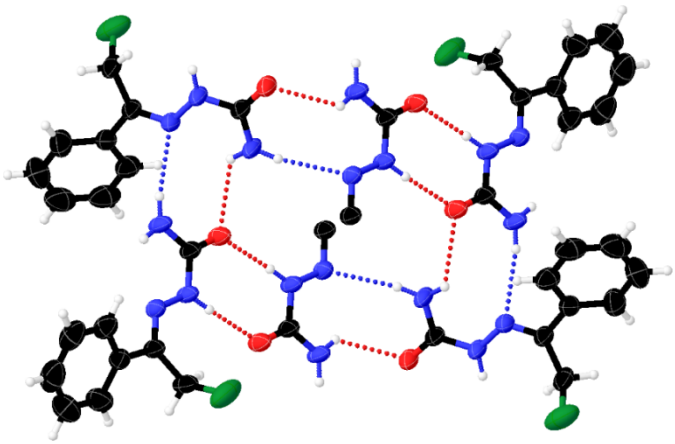

Figure 5. Ortep view of **1** showing 50% probability ellipsoids for atoms describing the $R_4^6(14)$ ring between two dimers and two molecules from two other dimers, both hydrogen bond interconnected [atom color code: H, white; C, black; N, blue; O, red; Cl, green]. For clarity, only one molecule from each of the two hydrogen-bonded dimers is fully represented. In the second molecule of each dimer, only the benzylic carbon atom is shown.

These $R_4^6(14)$ rings are fused with the existing $R_2^2(9)$ and $R_2^2(8)$ motifs, contributing to a dense and continuous two-dimensional hydrogen-bonded layer (Figure 6).The overall hydrogen-bonding pattern gives rise to a supramolecular sheet, which propagates parallel to the (100) crystallographic plane (Figures 6 and 7). Despite the presence of expanded hydrogen-bonding interactions, the supramolecular assembly shows limited growth along the crystallographic a-axis, indicating a pronounced layered character of the structure (Figures 6

and 7).The hierarchical organization of dimers, fused rings, and extended layers point up the critical role of directional N–H···O and N–H···N hydrogen bonds in growing the self-assembly and topological complexity of the crystal packing (Figures 6 and 7). This kind of hierarchical assembly into fused ring motifs is a recurring topology in recent hydrogen-bonded urea and semicarbazone derivatives [33, 34], affording a useful comparison with the layer-like framework observed for **1**.

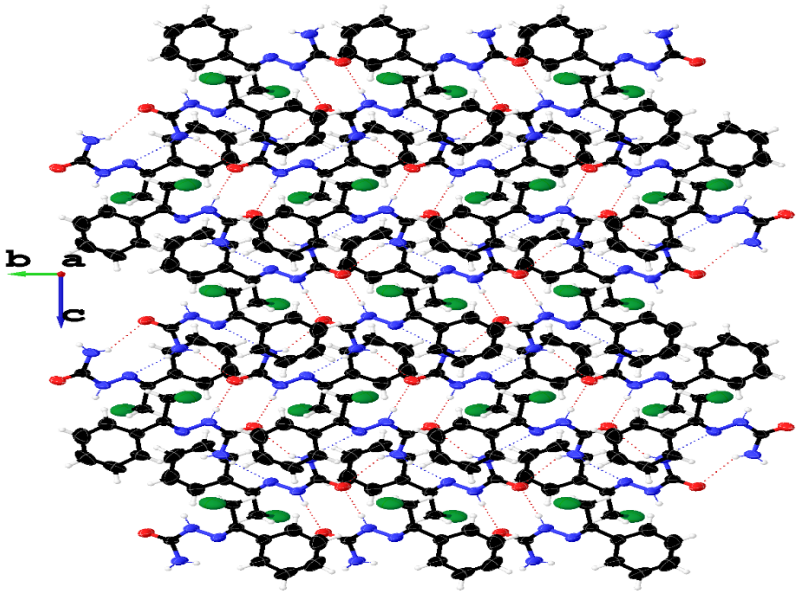

Figure 6. Ortep view of **1** (50% probability ellipsoids for atoms)layer-like structure along the (100) plane [atom color code: H, white; C, black; N, blue; O, red; Cl, green].

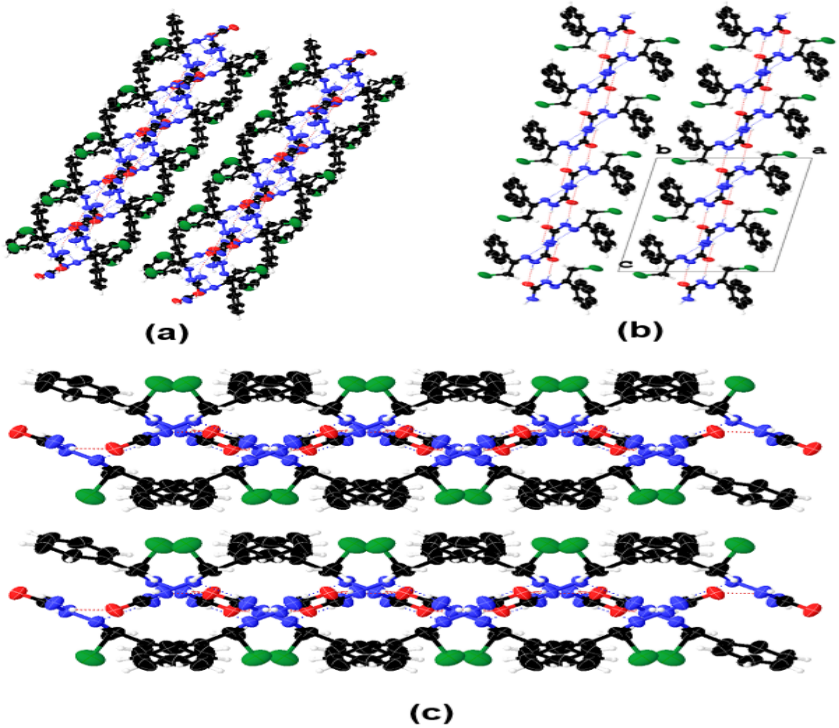

Figure 7. Ortep view of **1** (50% probability ellipsoids for atoms) showing the layers stacking along the (011) plane(a), along the (010) direction (b), and along the (001) direction (c) [atom color code: H, white; C, black; N, blue; O, red; Cl, green].

To gain further insight into the intermolecular interactions governing the crystal packing, a Hirshfeld surface analysis was performed using CrystalExplorer 21.5 [15]. The analysis enables quantitative assessment of close contacts between molecules by partitioning the crystal electron density into molecular fragments. The Hirshfeld surface mapped over d_{norm} (Figure 8(a)) reveals intense red spots near the carbonyl oxygen atom and around the N–H and NH_2 protons, indicating the presence of strong hydrogen-bonding interactions, consistent with the N–H···O and N–H···N contacts identified in the crystallographic analysis.

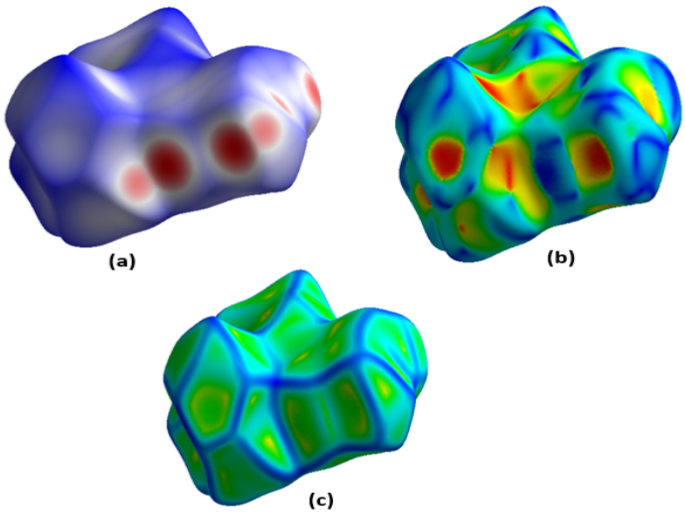

Figure 8. Hirshfeld surface of compound **1** mapped over d_{norm}(a),the Shape Index (b) and Curvedness (c), highlighting close intermolecular contacts. Red spots indicate regions of close contact in particular N–H···O and N–H···N hydrogen bonds, and the absence of π···π stacking.

The corresponding 2D fingerprint plots (Figure 3) provide a breakdown of the intermolecular contacts, with the relative contributions of various interactions. H···H contacts (32.7%) represent the largest contribution to the surface, a common feature in organic molecular crystals due to the ubiquity of hydrogen atoms and van der Waals interactions. However, these interactions are weak and non-directional. H···Cl/Cl···H interactions (20.1%) form the second-largest contribution, suggesting significant close contacts between the chloromethyl group and surrounding hydrogen atoms. This indicates the potential involvement of Cl as a weak acceptor in C–H···Cl interactions, which may contribute to local packing stability. H···C/C···H interactions (16.6%) reflect C–H···π or edge-to-face aromatic interactions, common in systems with aromatic rings and methyl/methylene groups. H···O/O···H contacts (14.9%) highlight the key role of hydrogen bonding between NH/NH_2 groups and the carbonyl oxygen, which are crucial for the formation of $R_2^2(8)$ and $R_4^6(14)$ motifs observed in the crystal structure.H···N/N···H interactions (9.1%) are also significant, and correspond to N–H···N hydrogen bonds involving the imine nitrogen as acceptor, contributing to the extended $R_2^2(9)$ ring. The absence of π···π stacking interactions is confirmed by the Hirshfeld surface analysis. The Shape Index map (Figure 8(b)) lacks the characteristic red/blue complementary patches, and the absence of extended flat areas within the Curvedness surface (Figure 8(c)), rule out significant face-to-face aromatic contacts.

These results corroborate the hydrogen-bonding motifs identified in the solid-state structure and display that, despite the dominance of dispersive H···H contacts, the directional H···O and H···N interactions are the main contributors to the supramolecular architecture.

4. Conclusion

In this study, the title semicarbazide–ketone hydrazone compound was successfully synthesized through a straightforward nucleophilic condensation of semicarbazide hydrochloride with α-chloroacetophenone under mild conditions. The structure of the compound was elucidated using ATR-FTIR and NMR spectroscopies, and single-crystal X-ray diffraction. The spectroscopic data provided clear evidence of the presence and chemical environment of all key functional groups, while the DEPT 135° confirmed the nature of the protonated and non-protonated carbon centers. Single-crystal X-ray analysis corroborated the molecular structure and revealed precise geometrical parameters in agreement with expected values for hydrazone and amide fragments. The crystal packing is governed by a rich hydrogen-bonding pattern involving N–H···O and N–H···N interactions, giving rise to discrete dimers, fused ring motifs $R_2^2(8)$, $R_2^2(9)$, and $R_4^6(14)$, and ultimately an extended two-dimensional supramolecular layer-like structure. Furthermore, the absence of π···π stacking interactions, as evidenced by Hirshfeld surface maps of the Shape Index and Curvedness, reinforces the dominance of directional N–H···O and N–H···N hydrogen bonds in stabilizing the crystal packing. This highlights the significant role of hydrogen bonding in shaping the supramolecular architecture of the compound. This type of compounds is not only valuable in medicinal chemistry because of their wide range of biological activities, but also serves as strategic building blocks in materials science, where their supramolecular behavior and electronic characteristics give incommensurate opportunities in chemosensing, optoelectronic and molecular recognition applications. The detailed structural insight described here contributes to a deeper comprehension of structure–property relationships in hydrazone- and urea-like materials and may, in the future, promote the rational design of homologous or related functional materials.

5. Conflicts of Interest

There are no conflicts to declare.

6. Acknowledgement

The authors gratefully acknowledge the Cheikh Anta Diop University (Senegal), the Aix-Marseille University and the Institute of Macromolecular Chemistry (Romania) for equipment facilities.

References

[1] Tapera, M., Kekeçmuhammed, H., Saripinar, E., Doğan, M., Tüzün, B., Koçyiğit, Ü. M., & Çetin, F. N. (2023). Molecular hybrids integrated with imidazole and hydrazone structural motifs: Design, synthesis, biological evaluation, and molecular docking studies. *Journal of Molecular Liquids, 391*(A), 123242. https://doi.org/10.1016/j.molliq.2023.123242

[2] Jabeen, M. (2002). A comprehensive review on analytical applications of hydrazone derivatives. *Journal of the Turkish Chemical Society, Section A: Chemistry, 9*(3), 663–698. https://doi.org/10.18596/jotcsa.1020357

[3] Carrasco, F., Hernández, W., Chupayo, O., Pumachagua, R., Spodine, E., Mosquera, J., Castro, O. N., Rodilla, J. M., Álvarez, C. M., & Dávalos, J. Z. (2024). Novel derivatives of phenylisoxazole-3/5-carbaldehyde semicarbazone: Synthesis, characterization, and computational studies. *Journal of Chemistry, 2024*, Article ID 8891272. https://doi.org/10.1155/2024/8891272

[4] Czyżewska, I., Mazur, L., & Popiołek, Ł. (2024). Transition metal complexes of hydrazones as potential antimicrobial and anticancer agents: A short review. *Chemical Biology and Drug Design, 104*(1), e14590. https://doi.org/10.1111/cbdd.14590

[5] da Cunha, P. S. T., Gini, A. L. R., Chin, C. M., dos Santos, J. L., & Scarim, C. B. (2025). Recent progress in thiazole, thiosemicarbazone, and semicarbazone derivatives as antiparasitic agents against Trypanosomatids and Plasmodium spp. *Molecules, 30*(8), 1788. https://doi.org/10.3390/molecules30081788

[6] Çapan, İ., Hawash, M., Qaoud, M. T., Gülüm, L., Tunoglu, E. N. Y., Çifci, K. U., Çevrimli, B. S., Sert, Y., Servi, S., Koca, İ., & Tutar, Y. (2024). Synthesis of novel carbazole hydrazine-carbothioamide scaffold as potent antioxidant, anticancer and antimicrobial agents. *BMC Chemistry, 18*, 102. https://doi.org/10.1186/s13065-024-01207-1

[7] Aljuhani, A. S., Nafie, M. S., Albujuq, N. R., Alsehli, M., Bardaweel, S. K., Darwish, K. M., Alraqa, S. Y., Aouad, M. R., & Rezki, N. (2025). Discovery of new benzothiazole 1,2,3-triazole hybrid based hydrazone/thiosemicarbazone derivatives as potent EGFR inhibitors with cytotoxicity against cancer. *RSC Advances, 15*(5), 3570–3591. https://doi.org/10.1039/D4RA07540D

[8] Kwon, O.-P., Jazbinšek, M., Yun, H., Seo, J.-I., Kim, E.-M., Lee, Y.-S., & Günter, P. (2008). Pyrrole based hydrazone organic nonlinear optical crystals and their polymorphs. *Crystal Growth & Design, 8*(11), 4021–4025. https://doi.org/10.1021/cg800218u

[9] Stegbauer, L., Schwinghammer, K., & Lotsch, B. V. (2014). A hydrazone based covalent organic framework for photocatalytic hydrogen production. *Chemical Science, 5*(7), 2789–2793. https://doi.org/10.1039/C4SC00016A

[10] Sakr, M. A. S., Sherbiny, F. F., & El Etrawy, A. A. S. (2022). Hydrazone based materials: DFT, NBO, MESP analysis and solar cell applications. *Journal of Fluorescence, 32*(5), 1857–1871. https://doi.org/10.1007/s10895-022-03000-6

[11] CrysAlisPro (Version 1.171.44.88a). (2025). *Rigaku Oxford Diffraction*.

[12] Sheldrick, G. M. (2015). SHELXT: Integrated space-group and crystal structure determination. *Acta Crystallographica Section A: Foundations and Advances, 71*(1), 3–8. https://doi.org/10.1107/S2053273314026370

[13] Sheldrick, G. M. (2015). Crystal structure refinement with SHELXL. *Acta Crystallographica Section C: Structural Chemistry, 71*(1), 3–8. https://doi.org/10.1107/S2053229614024218

[14] Dolomanov, O. V., Bourhis, L. J., Gildea, R. J., Howard, J. A. K., & Puschmann, H. (2009). OLEX2: A complete structure solution, refinement and analysis software. *Journal of Applied Crystallography, 42*(2), 339–341. https://doi.org/10.1107/S0021889808042726

[15] Spackman, P. R., Turner, M. J., McKinnon, J. J., Wolff, S. K., Grimwood, D. J., Jayatilaka, D., & Spackman, M. A. (2021). CrystalExplorer: A program for Hirshfeld surface analysis, visualization and quantitative analysis of molecular crystals. *Journal of Applied Crystallography, 54*(3), 1006–1011. https://doi.org/10.1107/S1600576721002910

[16] Wahbeh, J., & Milkowski, S. (2019). The use of hydrazones for biomedical applications. *SLAS Technology, 24*(2), 161–168. https://doi.org/10.1177/2472630318822713

[17] Popiołek, Ł. (2017). Hydrazide–hydrazones as potential antimicrobial agents: Overview of the literature since 2010. *Medicinal Chemistry Research, 26*(2), 287–301. https://doi.org/10.1007/s00044-016-1756-y

[18] Mathew, B., Suresh, J., Ahsan, M. J., Mathew, G. E., Usman, D., Subramanyan, P. N. S., Safna, K. F., & Maddela, S. (2015). Hydrazones as a privileged structural linker in antitubercular agents: A review. *Infectious Disorders – Drug Targets, 15*(2), 76–88. https://doi.org/10.2174/1871526515666150724104411

[19] Breitmaier, E., & Voelter, W. (1987). *Carbon-13 NMR spectroscopy: High-resolution methods and applications in organic chemistry and biochemistry* (3rd ed.). VCH Verlagsgesellschaft. https://doi.org/10.1002/jps.2600760918

[20] Badertscher, M., Bühlmann, P., & Pretsch, E. (2009). *Structure determination of organic compounds* (4th ed.). Springer. https://doi.org/10.1007/978-3-540-93810-1

[21] Silverstein, R. M., Webster, F. X., Kiemle, D., & Bryce, D. L. (2014). *Spectrometric identification of organic compounds* (8th ed.). Wiley.

[22] Ali, A., Khalid, M., Abdul Rehman, M., Anwar, F., Zain-Ul-Aabidin, H., Akhtar, M. N., Khan, M. U., Braga, A. A. C., Assiri, M. A., & Imran, M. (2020). An experimental and computational exploration on the electronic, spectroscopic, and reactivity properties of novel halo-functionalized hydrazones. *ACS Omega, 5*(30), 18907–18918. https://doi.org/10.1021/acsomega.0c02128

[23] Exner, O., & Böhm, S. (2002). Bond angles and bond lengths in monosubstituted benzene and ethene derivatives: A comparison of computational and crystallographic results. *Acta Crystallographica Section B: Structural Science, 58*(5), 877–883. https://doi.org/10.1107/S0108768102010510

[24] Esselman, B. J., Zdanovskaia, M. A., Owen, A. N., Stanton, J. F., Woods, R. C., & McMahon, R. J. (2023). Precise equilibrium structure of benzene. *Journal of the American Chemical Society, 145*(40), 21785–21797. https://doi.org/10.1021/jacs.3c03109

[25] Pisk, J., Đilović, I., Hrenar, T., Cvijanović, D., Pavlović, G., & Vrdoljak, V. (2020). Effective methods for the synthesis of hydrazones, quinazolines, and Schiff bases: Reaction monitoring using a chemometric approach. *RSC Advances, 10*(63), 38566–38577. https://doi.org/10.1039/D0RA06845D

[26] Vennila, S., Deepa, K., Nagaraja, K. S., Lakshmi, L., Selvaraj, S., & Karnan, C. (2024). Synthesis, structural, spectral, anticancer activity, and density functional theory investigations of 2-[hydrazinylidene(phenyl)methyl]pyridine. *Journal of Molecular Structure, 1316*, 138832. https://doi.org/10.1016/j.molstruc.2024.138832

[27] Bashir, M., Dar, A. A., & Yousuf, I. (2023). Syntheses, structural characterization, and cytotoxicity assessment of novel Mn(II) and Zn(II) complexes of aroyl-hydrazone Schiff base ligand. *ACS Omega, 8*(3), 3026–3042. https://doi.org/10.1021/acsomega.2c05927

[28] Zhang, Y., Sun, Y., Wang, T., Liu, J., Spingler, B., & Duttwyler, S. (2018). Synthesis and structural characterization of amidine, amide, urea and isocyanate derivatives of the amino-closo-dodecaborate anion [B12H11NH3]−. *Molecules, 23*(12), 3137. https://doi.org/10.3390/molecules23123137

[29] Saouli, S., Selatnia, I., Zouchoune, B., Sid, A., Zendaoui, S. M., Bensouici, C., & Bendeif, E. (2020). Synthesis, spectroscopic characterization, crystal structure, DFT studies and biological activities of a new hydrazone derivative: 1-(2,5-bis((E)-4-isopropylbenzylidene)cyclopentylidene)-2-(2,4-dinitrophenyl)hydrazine. *Journal of Molecular Structure, 1213*, 128203. https://doi.org/10.1016/j.molstruc.2020.128203

[30] Belskaya, N. P., Dehaen, W., & Bakuleva, V. A. (2010). Synthesis and properties of hydrazones bearing carboxamide, thioamide and amidine functions. *ARKIVOC, 2010*(i), 275–332.

[31] Kurbanova, M., Ashfaq, M., Tahir, M. N., Maharramov, A., Dege, N., Ramazanzade, N., & Cinar, E. B. (2023). Synthesis, crystal structure, supramolecular assembly inspection by Hirshfeld surface analysis and computational exploration of 4-phenyl-6-(p-tolyl)pyrimidin-2(1H)-one (PPTP). *Journal of Structural Chemistry, 64*(3), 437–449. https://doi.org/10.1134/S0022476623030095

[32] Parsaee, Z., Bahaderani, E. J., & Afandak, A. (2018). Sonochemical synthesis, in vitro evaluation and DFT study of novel phenothiazine base Schiff bases and their nano copper complexes as the precursors for new shaped CuO-NPs. *Ultrasonics Sonochemistry, 40*(A), 629–643. https://doi.org/10.1016/j.ultsonch.2017.08.010

[33] Ahmad, S., Khan, M., Rehman, N. U., Ikram, M., Rehman, S., Ali, M., Uddin, J., Khan, A., Alam, A., & Al-Harrasi, A. (2022). Design, synthesis, crystal structure, in vitro and in silico evaluation of new N′-benzylidene-4-tert-butylbenzohydrazide derivatives as potent urease inhibitors. *Molecules, 27*(20), 6906. https://doi.org/10.3390/molecules27206906

[34] Maluleka, M. M., & Mphahlele, M. J. (2024). Synthesis, crystal structure, cytotoxicity (MCF-7 and HeLa) and free radical scavenging activity of the hydrazones derived from 2-methylsulfonyl-5-nitrobenzaldehyde. *Results in Chemistry, 12*, 101896. https://doi.org/10.1016/j.rechem.2024.101896

[35] Muthuraja, P., Joselin Beaula, T., Shanmugavadivu, T., Bena Jothy, V., & Dhandapani, M. (2017). Hydrogen bonded $R_2^2(8)$ graph set in inducing charge transfer mechanism in guanidinium-3,5-dinitrobenzoate: A combined experimental, theoretical and Hirshfeld surface study. *Journal of Molecular Structure, 1137*, 649–662. https://doi.org/10.1016/j.molstruc.2017.02.067

Supplementary

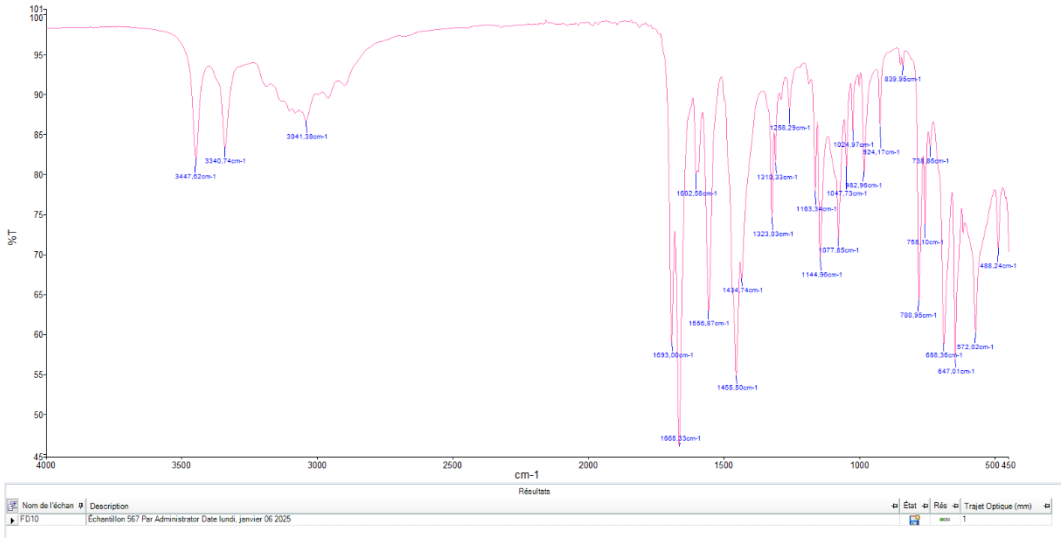

Figure S1. ATR-FTIR spectrum of compound **1**.

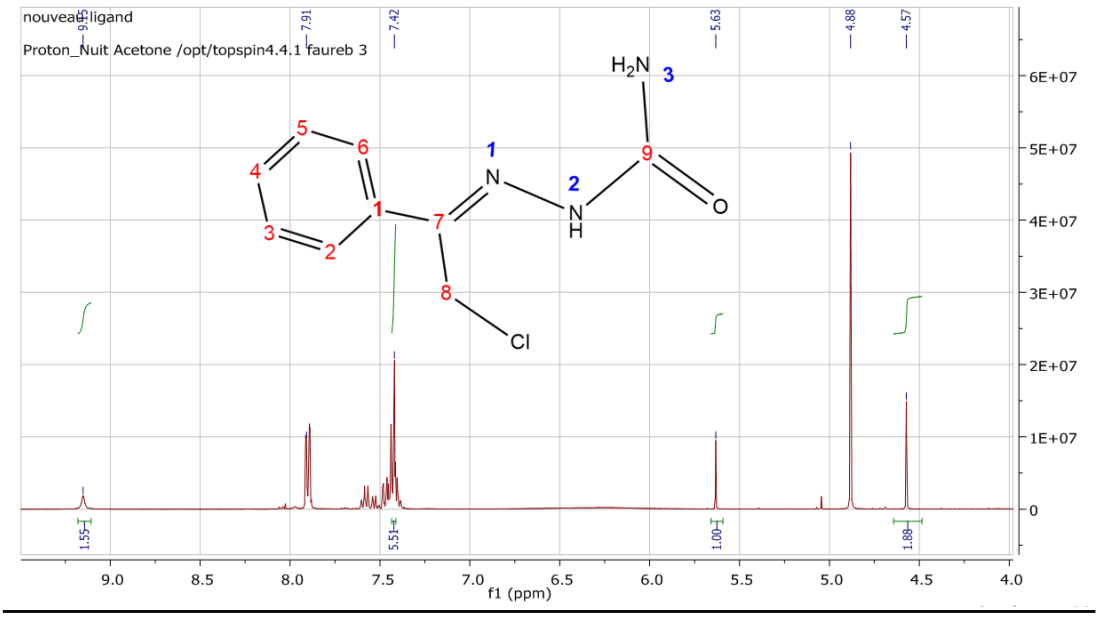

Figure S2. ^{1}H NMR spectrum of **1** dissolved in acetone.

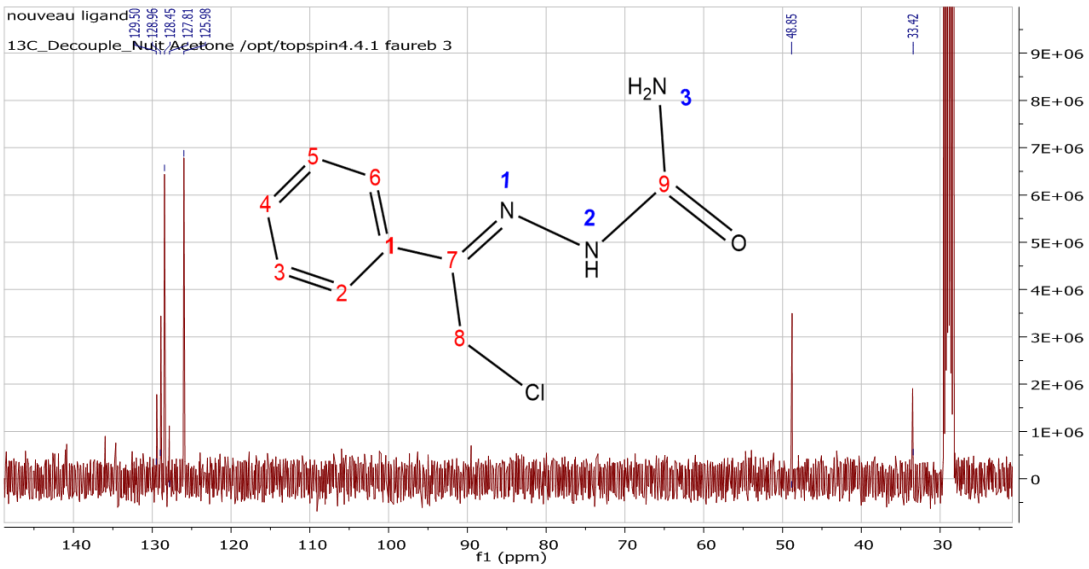

Figure S3. ^{13}C NMRspectrum of **1**dissolved in acetone.

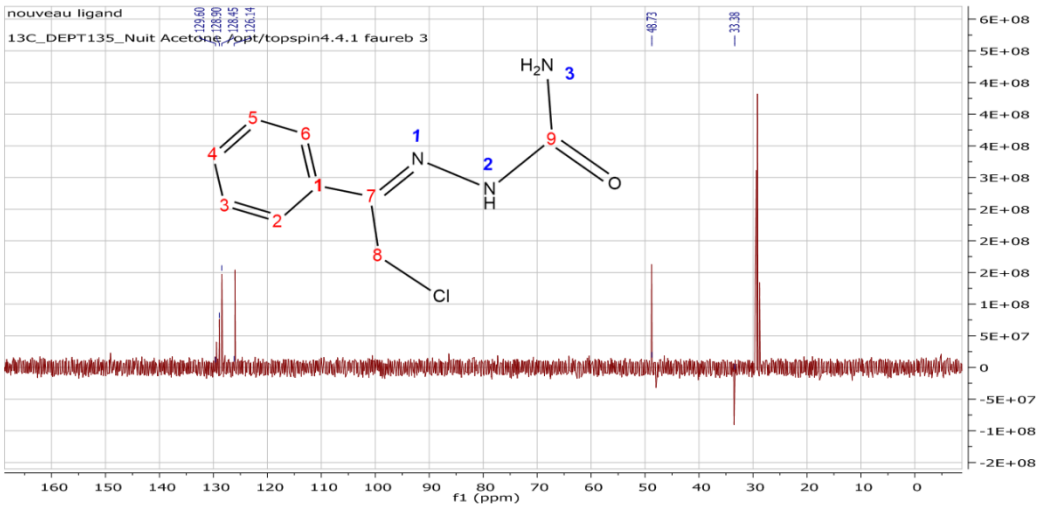

Figure S4. DEPT 135°spectrum of **1**dissolved in acetone.